Clim. Past Discuss., 9, 143–185, 2013
www.clim-past-discuss.net/9/143/2013/
doi:10.5194/cpd-9-143-2013

Climate of the Past Discussions

Modeling dust emission response to MIS 3 millennial climate variations from the perspective of East European loess deposits

A. Sima[1], M. Kageyama[2], D.-D. Rousseau[1,3], G. Ramstein[2], Y. Balkanski[2], P. Antoine[4], and C. Hatté[2]

[1]Laboratoire de Météorologie Dynamique, UMR8539, INSU-CNRS, & CERES-ERTI, Ecole Normale Supérieure, 24 rue Lhomond, 75231 Paris cedex 5, France
[2]Laboratoire des Sciences du Climat et de l'Environnement, UMR8212, CNRS-CEA-UVSQ, CE Saclay, l'Orme des Merisiers, Bât. 701, 91191 Gif-sur-Yvette cedex, France
[3]Lamont-Doherty Earth Observatory of Columbia University, Palisades, NY 10964, USA
[4]Laboratoire de Géographie Physique, UMR8591, CNRS – Université Paris I, place A. Briand, 92158 Meudon cedex, France

Received: 7 December 2012 – Accepted: 27 December 2012 – Published: 10 January 2013

Correspondence to: A. Sima (adriana.sima@lmd.ens.fr)

Published by Copernicus Publications on behalf of the European Geosciences Union.

Abstract

European loess sequences of the last glacial period (~ 100–15 kyr BP) show periods of strong dust accumulation alternating with episodes of reduced sedimentation, favoring soil development. In the western part of the loess belt centered around 50° N, these variations appear to have been caused by the North Atlantic rapid climate changes: the Dansgaard-Oeschger (DO) and Heinrich (H) events. It has been recently suggested that the North-Atlantic climate signal can be detected further east, in loess deposits from Stayky (50° 05.65′ N, 30° 53.92′ E), Ukraine. Here we use climate and dust emission modeling to investigate this data interpretation. We focus on the areas north and northeast of the Carpathians, where loess deposits can be found, and the corresponding main dust sources must have been located as well. The simulations, performed with the LMDZ atmospheric general circulation model and the ORCHIDEE land-surface model, represent a Greenland stadial, a DO interstadial and an H event respectively. Placed in Marine Isotope Stage 3 (~ 60–25 kyr BP) conditions, they only differ by the surface conditions imposed in the North Atlantic between 30° and 63° N. The main source for the loess deposits in the studied area is identified as a dust deflation band, with two very active spots located west–northwest from our reference site. Emissions only occur between February and June. Differences from one deflation spot to another, and from one climate state to another, are explained by analyzing the relevant meteorological and surface variables. Over most of the source region, the annual emission fluxes in the "interstadial" experiment are 30 to 50 % lower than the "stadial" values; they would only be about 20 % lower if the inhibition of dust uplift by the vegetation were not taken into account. Assuming that lower emissions result in reduced dust deposition leads us to the conclusion that the loess-paleosol stratigraphic succession in the Stayky area reflects indeed North-Atlantic millennial variations. In the main deflation areas of Western Europe, the vegetation effect alone determined most of the ~ 50 % stadial-interstadial flux differences. Even if its impact in Eastern Europe is less pronounced, this effect remains a key factor in modulating aeolian emissions

at millennial timescale. Conditions favorable to initiating particularly strong dust storms within a few hundred kilometers upwind from our reference site, simulated in the month of April of the "H event" experiment, support the identification of H events as layers of particularly coarse sedimentation in some very detailed profiles.

1 Introduction

Dust emission changes induced over Western Europe by the North-Atlantic millennial climate variation during Marine Isotope Stage 3 (MIS3, ~58 900–24 100 yr BP; Martinson et al., 1987) have been studied using an atmospheric general circulation model (Sima et al., 2009). The main aim was to test the correlation proposed by Rousseau et al. (2007) and Antoine et al. (2009) between sedimentation variations in aeolian sequences from the west of the European loess belt centered around the 50° N latitude, and the abrupt climate changes known as Dansgaard-Oeschger (DO) events (Dansgaard et al., 1993) and Heinrich (H) events (Heinrich, 1988; Broecker et al., 1992). The North-Atlantic cold episodes identified in ice or marine cores, i.e. Greenland stadials (hereafter GS; North Greenland Ice Core Project, 2004; Rousseau et al., 2006) and H events, were associated to periods of strong loess accumulation, indicating a very active dust cycle caused by dry and windy conditions. The warmer Greenland interstadials (hereafter GIS) were linked to moister and less windy conditions on the continent, with a less active dust cycle, favoring soil formation. Sima et al. (2009) have calculated emission fluxes over the main Western European deflation areas about twice as high during the cold North-Atlantic phases than during the warmer ones. Such changes were interpreted as explaining part of the millennial-timescale loess sedimentation variations revealed by the Western European aeolian sequences, thus, supporting the correlation suggested by data.

The European loess belt continues eastward, along the west–east aeolian corridor delimited, in glacial times, by the Fennoscandian ice sheet to the north and the relatively high mid-latitude European relief (including the Alpine glacier) to the south

(Fig. 1). Where the Carpathians curve southward, the loess band widens, covering a large part of the East European plain. Loess sequences from this part of the continent also reveal rapid environmental changes (Haesaerts et al., 2003; Rousseau et al., 2007, 2011; Gerasimenko and Rousseau, 2008; Antoine et al., 2009). These changes appear in the loess-paleosol stratigraphic succession, as well as in the variations of different indices: grain-size index, magnetic properties, carbon isotope ratios, and, where available, in the pollen record. Based upon these indices, a correlation was recently established between the loess sedimentation variations in Eastern and Western Europe (Rousseau et al., 2011). High-resolution data have been used from two key loess sequences: Nussloch, in Germany (Antoine et al., 2001, 2009; Rousseau et al., 2002, 2007), and Stayky, in Ukraine (Rousseau et al., 2011). These sequences are particularly detailed over the main loess sedimentation interval in Europe, ~40–15 kyr BP. Following investigations by Kukla (1977), a link between Central and Eastern Europe had already been shown on the basis of sequences from Dolni Vestonice, in the Czech Republic (e.g., Fuchs et al., 2012), and from another Ukrainian site, Vyazivok (Rousseau et al., 2001). Hence, it appears that the North Atlantic climate signal has been recorded throughout the European loess band, at least as far as 30° E. This data interpretation is the first aspect that we investigate here, by comparing simulated dust emissions north and northeast of the Carpathians (where the potential sources for the ~50° N aeolian deposits were most likely located), in the cold versus the warm North-Atlantic episodes.

While a reliable link can generally be established between stadial-interstadial climate changes and variations in sedimentation (and in other indices) for loess sequences with appropriate resolution, H events are much more difficult to distinguish. Studies on Chinese deposits have associated them to peaks in grain size (Porter and An, 1995), indicating a coarser sedimentation. The European loess deposits are considerably thinner than the Chinese ones. Nevertheless, for the high-resolution sequences of Nussloch and Stayky, it was also possible to associate two particular peaks in the respective grain-size index records to H events 3 and 2 (Rousseau et al., 2011). A coarser sedimentation implies an increased relative contribution of the local vs. remote dust sources

to dust deposition at the considered sites during H events, probably caused by brief, but particularly strong wind episodes (dust storms). This hypothesis is the second aspect that we examine using the modeling results.

The numerical simulations and the dust flux calculation method are the same as in Sima et al. (2009), therefore we only briefly describe them (Sect. 2). For Western Europe we knew the principal deflation area: the continental shelf exposed due to sea-level lowering, especially in the English Channel and the North Sea (Juvigné, 1976; Auffret, 1980; Auffret et al., 1982; Lautridou et al., 1985; Antoine et al., 2003a). For Eastern Europe we have changed our approach, because the main dust sources had yet to be identified. The dust calculations over the west of the continent have shown that, aside from the exposed continental shelf, the low relief areas north of approximately 48° N (where dust deposits are also located) have been subject to deflation as well. So, here we take as a reference the Stayky loess site (in Ukraine), where millennial-timescale variations are particularly well recorded, and identify the potential sources for the dust deposited around this site (Sect. 3.1). Taking into account what we have learned on the strong seasonality of emissions in the Sima et al. (2009) study, we first determine the "dusty season" in these source areas (Sect. 3.2), and then analyze the relevant climate variables and surface conditions simulated over this period of the year (Sect. 3.3). We pay special attention to the vegetation, which inhibits aeolian erosion. Stadial-interstadial vegetation changes were identified in our previous work as the main factor by which the North-Atlantic millennial variations modulated dust emission in the western European deflation areas. We discuss our results (Sect. 4), draw the conclusions and indicate some perspectives (Sect. 5).

2 Reference loess site, numerical simulations, dust emission calculations

The reference loess site for this study is Stayky (50° 05.65′ N, 30° 53.92′ E, 194 m a.s.l.), in Ukraine, located by the Dnieper River, about 50 km south of Kiev. This outcrop was chosen for its detailed record of the last climate cycle, during a preliminary investigation

of the numerous outcrops of the loess series studied in the area (Gerasimenko and Rousseau, 2008). It is situated on a cliff ending the plateau on the right bank of the river; the Dnieper river floodplain lies on the left bank. The sequence corresponding to the last climatic cycle has been studied at high resolution by defining a precise stratigraphy, sampling continuously for grain-size analysis, and taking sediment for optically stimulated luminescence (OSL) dating (Rousseau et al., 2011). For the interval 38 to 18 kyr BP, alternating loess and embryonic soils similar to the loess-paleosol doublets observed at Nussloch (Germany) have been identified, as well as a similar pattern of the grain-size index variations. It was shown that the loess-embryonic soil doublets correlated with Greenland stadial-interstadial climate changes. Also, it was suggested that two particular peaks of the grain-size index corresponded to H events 3 and 2.

The simulations have been carried out with the LMDZ.3.3 atmospheric general circulation model (Jost et al., 2005) including the ORCHIDEE land-surface model (Ducoudré et al., 1993; Krinner et al., 2005). They represent a reference glacial state (Greenland "stadial", GS), a cold ("H event", HE) and a warm ("Dansgaard-Oeschger", or "Greenland interstadial", GIS) perturbation, and are designed to resemble the GS9-H4-GIS8 sequence around the H4 event (approx. 39 kyr BP; Bard et al., 2004). Thus, the orbital parameters (Berger, 1978; Berger and Loutre, 1991) are set to 39-kyr BP values. The CO_2 concentration is 209 ppmv (Petit et al., 1999). The ice-sheet configuration at 14 kyr BP is selected from the ICE4G reconstruction (Peltier, 1994), as corresponding to a sea level similar to that at 39-kyr BP, approximately 60 m lower than today (Siddall et al., 2008). The land-sea mask of the LMDZ and SECHIBA models is adapted to this sea level. In the absence of reconstructions for the MIS3 sea-surface temperatures (SSTs) and sea ice, the GLAMAP2000 reconstruction (Sarnthein et al., 2003) for the Last Glacial Maximum (LGM, approximately between 23 and 18 kyr BP) is used in the reference glacial climate simulation GS. The cold and warm perturbations are obtained by only altering the North Atlantic surface conditions in the latitudinal band between 30° N and 63° N. All-year-long zonal SST anomalies of up to ±2 °C (Cortijo et al., 1997) are applied in this band, and sea ice is imposed where the SST is lower than −1.8 °C.

In the ORCHIDEE model version used here (Krinner et al., 2005), the computed leaf area index (LAI) varies between minimum and maximum values fixed for each plant functional type (PFT) to standard values based on averaged observations, and is only modulated by the AGCM-derived temperature. The maximum grid-cell fraction that can be occupied by each PFT is also prescribed. In our paleoclimate experiments we keep the present-day values, as recommended by the Paleoclimate Modelling Intercomparison Project (e.g., Braconnot, 2004) for the LGM simulations. The actual grid-cell fraction covered by a PFT depends on the imposed maximum vegetation fraction and the computed LAI. In each experiment, the LMDZ-ORCHIDEE model is run for a spin-up period of one year, followed by 20 yr that are analyzed.

The Sima et al. (2009) study has shown the importance of vegetation, as an inhibitor of aeolian erosion, in modulating dust emission at millennial timescale in the western european deflation areas. Therefore, here we calculate again separately the emitted "dry" dust flux F_d, taking into account all factors but the vegetation effect. These fluxes are given by the following formulas:

$F_d = C' \cdot f_d \cdot w_{10m}^2 \cdot (w_{10m} - w_{th})$ for $w_{10m} > w_{th}$ ($F_d = 0$ otherwise)

and

$F = F_d \cdot f_v = C' \cdot E \cdot w_{10m}^2 \cdot (w_{10m} - w_{th})$ for $w_{10m} > w_{th}$ ($F = 0$ otherwise)

where :

- C' is a constant for every grid cell that only depends on intrinsic characteristics as the surface roughness (vegetation excluded), grain-size distribution and texture of the bare soil. Here we take $C' = 5 \times 10^{-7}\,\mathrm{g\,m^{-5}\,s^2}$ everywhere in our domain of study, an intermediate value in the range of those determined by Balkanski et al. (2004) for the present-day arid and semi-arid regions;
- f_d, which we call "dry soil fraction", quantifies the soil water effect on dust emission. It equals the snow-free fraction of the grid cell if the soil is dry over more than 5 mm depth, and is 0 otherwise;

- f_v, the vegetation factor, quantifies the vegetation effect of inhibiting wind erosion. It is calculated as a function of the vegetated soil fraction f_{veg}, following the Eq. (6) of Fryrear (1985), corrected at low (< 10 %) and high (> 60 %) vegetation cover:

  $f_v = \min(1, 1.81 \cdot \exp(-7.2 \cdot f_{veg}))$ if $f_{veg} < 0.6$, and $f_v = 0$ otherwise.
- $E = f_d \cdot f_v$ is the "erodible fraction", and represents the grid-cell fraction where dust emission is allowed at any given moment by both soil humidity and vegetation effects;
- w_{10m} is the 6-hourly averaged 10 m-wind computed by the atmospheric model;
- w_{th} is the threshold wind speed for erosion, determined for each grid cell, same as C', by the intrinsic (bare) soil characteristics. As in Sima et al. (2009), a constant value is used everywhere: $7\,\mathrm{m\,s^{-1}}$, close to the lowest values for the present-day deserts, either measured (Wang et al., 2003) or derived as a function of soil characteristics (Marticorena and Bergametti, 1996; Laurent et al., 2005).

3 Results

3.1 Potential dust sources

In order to determine where the main source areas must have been located with respect to the Stayky loess site, we analyze the wind direction at the surface and in altitude. We take the 850 hPa level (corresponding on average to an altitude of about 1500 m a.s.l.) as relevant for the medium-to-long distance dust transport. The mean annual wind direction at this level has a strong westerly component in the reference state (Fig. 2), as well as in the two perturbations (Rousseau et al., 2011, Fig. 5 therein). To identify the most probable position of the local source areas with respect to the site, we examine the wind roses derived from 6-hourly 10 m-winds for the 20 yr analyzed for each simulation (Fig. 3). Again, in all three states, westerly wind occurrences greatly

exceed the easterly ones. This explains why, despite the large amount of sand available in the Dnieper river floodplain, east of Stayky, very little sand is found in the loess deposit (Rousseau et al., 2011). Also, the loess site is located approximately 150 meters higher than the valley, so the sand in the loess profile must have been transported during rare strong easterly wind events. The 10 m-wind speed values are up to 20 $m\,s^{-1}$ for the GS state, up to 21 $m\,s^{-1}$ for GIS, and about 22 $m\,s^{-1}$ for HE, but the frequency of strong winds, exceeding 14 $m\,s^{-1}$, is not high enough to see it in the plots. According to Sima et al. (2009), the yearly averaged dust fluxes are not controled by the strongest winds, but rather by the much more frequent medium wind-speed category (from 9 to 14 $m\,s^{-1}$ in the case of the western European main sources). For HE, the strongest 10 m-wind events, exceeding 20 $m\,s^{-1}$, occur in April and December (not shown). We will discuss this result in Sect. 3.2, where we look at dust emission seasonality and the relationship with the identification of H events in loess sediments as peaks of grain-size index. Finally, considering the low end of the grain-size range in the Stayky profile (the clay fraction, with diameters of less than 4.6 microns), most of the constituting material has probably originated from sources not more than thousand km far from the site (Rousseau et al., 2011). All these taken into account, we consider that the main potential dust sources for Stayky must have been located between 15° and 35° E. This is the longitudinal range for which we will perform the dust emission calculations. The latitudinal range of interest spans over a 10°-wide band centered on Stayky: from 45° N, the latitude of the southern Carpathians, to 55° N, in the Baltic Sea, and close to the Fennoscandian ice-sheet southern limit on the continent around 40 kyr BP (~ 57° N in our experimental setup). The resulting domain is shown in Fig. 2. When representing dust fluxes or surface conditions, we exclude the Carpathians (by masking the areas with altitudes exceeding 500 m), where no relevant emission may occur. We also exclude the lowlands inside the mountain arch, as they are unlikely to have contributed to dust deposition in the ~ 50° N band examined in this study.

For each simulated climate state, we compute yearly averaged dust emission fluxes over the domain of interest (Fig. 4). In all climate states, emission mainly occurs in

a NW–SE band, located north and northeast of the Carpathians (Fig. 5). Two spots appear as most active with respect to climate-related conditions and are placed west–northwest of Stayky, constituting potential source areas for this reference site. The one closest to Stayky, hereafter referred to as "Spot 1", is in Ukraine, centered at about 51° N–26° E (S1 in Fig. 4a). It partly covers areas where loess deposits are located (Fig. 5), which means that here dust remobilization might have been important. The second most active region, "Spot 2", is in Poland, centered at about 53° N–19° E (S2 in Fig. 4a).

The extent of the potentially most active sources does not change significantly from the GS to the HE climate state (Fig. 4a, b), but annual mean dust fluxes are smaller for HE than for GS, especially over Spot 2. A shrinking of the potential emission area can be seen for the GIS compared to GS, as well as a decrease, stronger than in the HE case, of the annual mean dust emission fluxes (Fig. 4c).

To explain the spatial distribution of the potential deflation areas and the differences of dustiness between the simulated climate states (Fig. 4), we need to examine the variations of the relevant climate variables: wind, precipitation, temperature, as well as the surface conditions determined by these variables: soil humidity, snow and vegetation covers. The annual or seasonal means of these quantities are not quite relevant for this matter (see Sima et al., 2009), so we first determine the period of the year when dust emission occurs over our area of study, and then analyze the variables of interest as averages on this period.

3.2 Seasonality of emissions

Sima et al. (2009) have shown the strongly seasonal nature of dust emission occurrence over the large deflation areas formed by sea-level lowering in the English Channel and the south of the North Sea. Here we remain in the same latitude range, and the annual cycle of the main variables impacting dust emission resembles that for the west of Europe (Fig. 5a, b in Sima et al., 2009). Winter is characterized by strong winds and scarce vegetation, but snow cover and the high soil humidity prevent dust from being

uplifted. Conversely, in summer the wind weakens and, as the soil dries up, the development of vegetation becomes the main surface process blocking dust mobilization. These different conditions constraining dust emission determine the potential deflation areas, and their seasonality. Thus, in our domain of interest, the main emission band located north and northeast of the Carpathian Mountains is most active in springtime, when a compromise is reached between soil humidity, wind and vegetation conditions (Fig. 6). As in the western European source areas, the seasonal evolution of dust emission intensity differs from a climate state to another. Furthermore, for each climate state, the two most active spots show noticeable differences in their seasonality. Spot 1 is the first to start emitting dust: in February for GS and GIS, and in March for HE. In all three states, the most active period is April. The conditions become unfavorable to dust emission in May for GIS, and in June for the other two states.

Spot 2 has the same general evolution, but with one month of delay with respect to Spot 1. It starts to significantly emit in March for GS and GIS, and in April for HE. For GS and HE it is most active in May, and stops emitting in June, whereas for GIS the emissions cease one month earlier.

If we consider the two most active areas together, the dusty season in our region of interest lasts from February to June in the stadial state, from March to June in the HE state, and from February to May in the interstadial state. For all months and climate states the average 850 hPa winds are from west or west–northwest (Fig. 6), so that the deflation band we have identified may feed the European aeolian deposits located farther eastward (Fig. 1). Considering the distance to our reference site ($\sim$ 300 km for Spot 1, $\sim$ 800 km for Spot 2), and the monthly means of 850 hPa-wind direction over the emission season, Spot 1 is the best candidate as a dust source for the loess deposits in the Stayky area. Spot 2 certainly contributes as well, even though (again, considering the monthly means of 850 hPa-wind direction in Fig. 6) much of the dust emitted here is probably transported on a more northern path.

3.3 Climate variables, surface conditions and dust emission

To explain the spatial distribution of the potential deflation areas, the differences of dustiness and seasonality between the two most active spots, and between the simulated climate states (Figs. 4 and 6), we need to examine the relevant climate variables and surface conditions. As shown in Sect. 3.2, for all simulated climate states, the annual amount of dust is only produced over a period between February and June. Therefore, in the following, we analyze the variables and anomalies of interest as averages over this "dusty season".

The climate variables we address are (Fig. 7): (i) 2 m-temperature, which impacts soil humidity (through evaporation), snow cover extent and duration, and vegetation development; (ii) precipitation, which in our study only impacts soil humidity and snow cover, not vegetation (cf. Sect. 2.1), and (iii) 10 m-wind, on which dust emission fluxes strongly depend (cf. Sect. 2). For the surface conditions, we examine (Fig. 8): the dry fraction f_d, the vegetation factor f_v and the resulting erodible fraction $E = f_d \cdot f_v$

3.3.1 The reference GS state

We focus on the domain for which we performed the dust calculations: 45°–55° N, 15°–35° E, and on the resulting dust emission band shown in Fig. 4. In the reference GS state, the average temperature over the investigated domain follows a north-south gradient, with values ranging approximately from -4° to 6 °C (Fig. 7a). This leads to a faster snow melting and an enhanced surface evaporation in the southeast (SE) part compared to the northwestern (NW) part of the emissions band (not shown). Precipitation averages are between 1 and 1.5 mm day^{-1}, a bit lower in the SE (Fig. 7d). These combined factors give better conditions for emission with respect to soil humidity in the SE of the band. Thus, the calculated surface dry fraction f_d is between 50–70 % in this region, and decreases to only 20–40 % in the NW part (Fig. 8a).

In our simulations, vegetation development is only determined by temperature. Hence the onset of the growth season starts later in the NW of the emission band.

Thus, on average over the February to June interval, the vegetation inhibiting effect is less effective in the NW of the emission band (mean vegetation factor $f_v > 0.7$) than in the SE ($f_v < 0.5$) (Fig. 8d). The two spots clearly appearing in Fig. 4a as preferential emission areas have high f_v values: 0.6–0.7 for Spot 1, and more than 0.7 for Spot 2. When calculating the erodible fraction E (Fig. 8g), combination of f_d and f_v, the gradient in the dry fraction of the surface, f_d, prevails. Thus, on average over the dusty season, E is lower in the NW of the deflation band (10–15 % in Spot 2) than in the SE (15–20 % in Spot 1 and more than 25 % south of Stayky).

Dust emission fluxes depend on the erodible fraction and the cube of 10 m-wind speed, combined at fine timescale (6 h in our case). The average 10 m-wind speed increases from less than 5 m s^{-1} in the SE to more than 6 m s^{-1} in the NW (Fig. 7g). This increase prevails in the flux calculation over the decrease of E, resulting in stronger dust emission in the NW than in SE of the deflation band. Thus, as shown in Fig. 4, more dust is emitted in Spot 1 then in Spot 2 on average over the year (or over the dusty season; the total amount is practically the same). Both spots can be identified in Figs. 7d and 7g as areas of relatively high 10 m-wind speed and low precipitation in our investigated domain. The region of relatively high erodible fraction (25–30 %) south of Stayky does not correspond to high emission, because the wind is not strong enough.

The differences of seasonality between Spots 1 and 2 (Fig. 6) can also be explained by considering the spatial distribution of temperature and precipitation averaged over the dusty season (Fig. 7a,d), and the general evolution in the investigated area of the wind speed, soil humidity (both decreasing from winter to summer) and vegetation cover (better developed in summer than in winter). In all states, it is colder in Spot 2 than in Spot 1, located more to the south, while the average precipitation amount is quite similar. Considering the temperature impact on soil humidity and vegetation, this explains why the emission period is delayed in Spot 2 compared to Spot 1 (by 1 month; Fig. 6). It also explains why in the cold GS and HE states Spot 2 is most active a month later than Spot 1, in May, in spite of the gradual decrease of the average 10 m-wind from winter to summer. The wind weakening is compensated for by a combination of drier

surface and vegetation developing later than in Spot 1 (where the maximum emission is in April).

3.3.2 Changes of climate and surface variables in the "H event"-like cold perturbation, and consequences on dust emission

In the HE experiment, the lower North-Atlantic SSTs imposed in the latitudinal band 30°–63° N result in an average cooling over the dusty season of 0.5 to 2 °C in our investigated domain (Fig. 7b), the anomaly being strongest in its W-NW part. Precipitation only locally decreases, and by a small amount compared to the reference GS state (Fig. 7e). The combination of these two factors increase the contrast in soil humidity between the NW and the SE of the emission band, compared to GS (Fig. 8a, b). Thus, the dry fraction f_d decreases by up to 8 % in the NW, but increases in the SW by up to 6 % (Fig. 8b).

In our experiments, a delay in vegetation development and lower average vegetation cover than for GS are straightforward consequences of the lower HE temperatures. Thus, the vegetation factor f_v (anti-correlated with the vegetated soil fraction, as defined in Sect. 2) is everywhere slightly higher than for GS (Fig. 8e). The resulting erodible fraction anomaly is positive almost everywhere (Fig. 8h). The surface conditions are thus better for deflation than in the GS state, but the average wind slightly decreases compared to GS over most of the deflation band (Fig. 7h). The combined effect (at fine timescale, here 6 h) of these opposing variations on the dust emission change between HE and GS is contrasted along the deflation band: from a strong decrease in the NW to a slight increase in the SE (Fig. 9e). The HE fluxes are 50–80 % of the GS ones in Spot 2, and 70–100 % in Spot 1. Both spots are still well identified as the most active areas in the deflation band, with yearly average dust fluxes of up to 120 g m^{-2} yr^{-1} (Fig. 4b). The relative increase of emission fluxes south and east of Stayky is due to the increase of the erodible fraction by more than 4 %, in a zone where E was already high for GS (20–25 %). Nevertheless, due to relatively weak winds, the dust fluxes remain low (< 60 g m^{-2} yr^{-1}).

3.3.3 "Stadial-Interstadial" changes of climate and surface variables, and impact on dust emission

We now analyze the effect of a North-Atlantic SST increase similar to that associated with a Dansgaard-Oeschger warming event. The imposed SST perturbation results in an average temperature increase from 1.5° in the SE of our investigated domain to more than 3 °C in the NW (Fig. 7c). As in the case of the cold perturbation, there is little change in precipitation (Fig. 7f). The resulting f_d anomaly is positive almost everywhere in the emission band (Fig. 8c), and higher in the NW (more than 8 %) than in the SE (up to about 4 %). This anomaly distribution reduces the SE–NW contrast of f_d compared to the GS state.

The warmer climate favors vegetation development, so that the vegetation factor f_v decreases everywhere in the domain, by 0.1 to 0.2 in the emission band (Fig. 8f).

The resulting E anomaly is also negative everywhere (Fig. 8i). The average 10 m-wind speed decreases as well, more in the NW than in the SE of the domain, which attenuates the NW–SE wind-speed gradient along the emission band compared to the GS state (Fig. 7i). All these lead to a general decrease of the emission fluxes, which are now mostly between 40–100 $g\,m^{-2}\,yr^{-1}$ in the main spots, about half of the GS values (80–160 $g\,m^{-2}\,yr^{-1}$). The decrease is stronger than in the HE experiment in the eastern half of the band, including Spot 1 (Fig. 4c).

3.3.4 The contribution of vegetation in modulating dust emission during the North-Atlantic abrupt changes

The Sima et al. (2009) study has shown that, for the main deflation areas of Western Europe, stadial-interstadial changes in wind, precipitation, soil moisture and snow cover did not produce changes in dust emission as important as indicated by the sedimentation changes seen in the loess profiles. It was mainly the vegetation, by its effect of inhibiting the aeolian erosion, which modulated the dust emissions in response to climate variations. The inhibition was considerably more effective in the relatively warmer

GSI state (due to a better developed vegetation) than in the cold GS and HE states. In order to assess the importance of this mechanism in the area investigated here, further away from the North Atlantic region, in which the abrupt climate changes originate, we analyze annual mean emission flux ratios HE/GS and GIS/GS in the absence (F_d, Fig. 9a–c) and in the presence of the vegetation effect (F, Fig. 9d–f).

When only taking into account the effects of surface wind and precipitation (including soil humidity and snow cover), dust emission occurs almost everywhere in our domain (Fig. 9a). Annual mean dust fluxes (F_d) in GS locally exceed 220 $g\,m^{-2}\,yr^{-1}$ in the two most active spots. The HE/GS and GIS/GS flux ratios are quite similar in our band of interest, mostly between 80–100 % (Fig. 9b,c), meaning there is little difference between the perturbed and reference states. In the GIS case, these values are too high to be reconciled with the strong stadial-interstadial deposition differences indicated by the loess record. Locally, they are even higher than those for the cold HE perturbation. When adding the vegetation effect in the dust flux computation, the GS annual mean dust fluxes (F) strongly decrease compared to F_d (Fig. 9d). The values in our two main spots are now generally between 80–160 $g\,m^{-2}\,yr^{-1}$. The band north and northeast of the Carpathians clearly appears as the main emission area. Here, the HE/GS flux ratio does not change much: an increase of about 10 % can be seen especially in the eastern part of the domain (Fig. 9e). On the contrary, in the GIS case, a shrinking of the deflation area and a significant reduction of fluxes can be seen (Fig. 9d). The flux reduction is strongest in the most active spots, where GIS fluxes are now 50–70 % of the GS ones, in better (qualitative) agreement with the loess data.

The considerable difference between annual mean emission fluxes without (F_d, Fig. 9a) and with vegetation effect (F, Fig. 9d) is mainly due to the shortening of the emission season, as shown by the F_d and F annual cycle averaged over each of the main Spots (Fig. 10). Without vegetation, emission would occur all the year round, whereas taking the vegetation effect into account restrains the emission to late winter and springtime. The same was true for the main deflation areas of Western Europe: the English Channel and the south of the North Sea (Sima et al., 2009, Fig. 5c therein).

There are also some differences. In the western European areas, in all three simulated states, the monthly mean F_d was highest in May, month during which the attenuation of emission by the developing vegetation was also strong. Taking this effect into account resulted in a maximum emission flux F in April for GIS and GS. In Spot 1, F_d has similar values over the dusty season for the three states, and reaches its maximum in April, one month earlier than at the western sources. The vegetation effect in this month is considerably weaker here than in the western sources (so that the maximum of emission flux F remains in April), but is strong enough to differentiate the warm perturbation from the cold states. Spot 2 is in an intermediary situation: both F_d and F reach their maximum in May for GS and HE, and in April for GIS. F_d is higher for GIS than for HE, and both are smaller than for GS. It is the vegetation effect that makes the GIS fluxes become smaller than the HE ones.

4 Discussion

Our climate simulations and dust calculations certainly bear some limitations. In the few years since we have run them, new efforts have been made towards better understanding various aspects of the abrupt climate changes, for example, the sub-millennial structure of DO events (e.g., Capron et al., 2010), the mechanism of stadial-interstadial oscillations (e.g., Arzel et al., 2012) or the Heinrich event scenario (Alvarez-Solas and Ramstein, 2011). Still, when it comes to simulating HE, GS and GIS states with an AGCM, the lack of sufficiently precise information persists, so that numerical setups are idealized in a number of aspects. Thus, in our study, LGM SSTs and sea-ice extent are imposed for the reference "stadial" state, which otherwise is designed to correspond to 39 kyr BP. Also, these sea-surface conditions follow a seasonal cycle, but which does not change from one year to another. This lack of interannual variability in the boundary conditions could affect the representation of extreme wind events. The SST anomalies we apply in the North Atlantic in order to obtain the DO- and H event-like perturbations are also highly idealized and only depend on latitude. No change of ice-sheet

size and extent (and consequent adjusting of sea level) associated with the DO and H events are represented. Nevertheless, as thoroughly discussed in Sima et al. (2009), our experiment design allows us to test the impact on dust emission of changes in the sea-surface conditions as those suggested by data for DO and H events.

The relatively small differences of average wind and precipitation between the simulated climate states are a consequence of the imposed zonal SST anomalies of only up to 2 °C. While the maximum anomaly of 2 °C is set according to data, a more realistic distribution of SST anomalies and of the resulting sea ice might increase these differences. However, they would probably still not reach those obtained in other numerical experiments employing very contrasted boundary conditions between stadials, interstadials and H events (e.g., Hostetler et al., 1999; Renssen and Bogaart, 2003)

For forthcoming AGCM studies, an alternative to using reconstructed SSTs and prescribed perturbations would be to employ the output of a coupled global climate model (atmosphere–ocean–sea ice–land), after regridding at the finer resolution generally required for the AGCM. This would solve the interannual variability issue, and provide a less idealized distribution of SST anomalies. Even if it also comes with the climate model biases in simulating the sea surface conditions, this alternative is certainly worth exploring, especially since coupled atmosphere–ocean–sea–ice general circulation model experiments have started to address the MIS3 period (Merkel et al., 2010; Brandefelt et al., 2011).

An important limitation of our simulations concerns the vegetation treatment. In the main deflation areas of Western Europe we have imposed a glacial-type vegetation consistent with available paleodata (e.g. Woillard, 1978; de Beaulieu and Reille, 1984, 1992; Rousseau et al., 1990; Hatté et al., 1998; Peyron et al., 1998; Müller et al., 2003; Hatté and Guiot, 2005; Moine et al., 2008), only composed of boreal evergreen needleleaf trees (up to 1 % of a grid cell) and C3 grass (up to 80 %). In the Eastern Europe, the maximum fractional cover and the LAI limits for each PFT are prescribed to present-day values, as for the LGM PMIP experiments. As mentioned by Woillez et al. (2011), the present-day European vegetation includes considerable areas of agricultural grass,

therefore the landscape is not so different from the glacial one, mainly represented by steppe or steppe-tundra. In our simulations, trees occupy less than 10 % of any given grid cell of the main emission band (Fig. 9d). Grass takes on average on the dusty season 20–35 % of each grid cell in the GS state, 25–50 % in the GIS state and 15–25 % in the HE state, the rest of the cell being left to bare soil. Such vegetation composition seems reasonable for the time slice we approach, at about 40 kyr BP, compared to the steppe or steppe-tundra predominating in Europe at the LGM. In the NE of the domain, outside of the main band, some dust emission would occur as well if vegetation were not accounted for (Fig. 9a). Here, grid cells are occupied all-year-long by up to 30 % trees. For the cold Greenland episodes, this might be an overestimation, but we think it has no significant impact on our results: the differences between the dust fluxes calculated without vs. with vegetation effect (Fig. 9) are the direct consequence of the fact that each grid cell is partly covered by vegetation, no matter whether trees or grass (an effect expressed by the vegetation factor f_v). Also, even for the warmest simulated state, GIS, the total vegetation fraction averaged over the dusty season does not exceed 50 % of a grid cell in most of the domain investigated here, which is still coherent with a steppe-tundra environment.

The adjustment of vegetation to the climate conditions is only determined by temperature in the configuration of ORCHIDEE used in this study. The glacial climates we investigate were not only colder, but also drier than today in our area of interest. More realistic simulations should also include the precipitation impact on vegetation, as well as the effect of a lower atmospheric CO_2 concentration in glacial times than today. However, it is difficult to validate simulated vegetation over our area of interest for the main loess sedimentation period, due to the scarcity of pollen records compared to other parts of Europe or glacial time slices. In the frame of the Stage 3 project (Barron and Pollard, 2002), palynological data compiled from the four sites falling in our investigated domain suggest tundra and temperate grassland around 50° N–20° E for the interstadials, but give no information for the stadials (Huntley et al., 2003, et references therein). For the Stayky area (approx. 50° N–30° E), Gerasimenko and Rousseau (2008) indicate

a transition from a forest-steppe environment before ∼ 40 kyr BP to steppe during the main loess sedimentation period, with arboreal pollen varying between ∼ 10 % in the loess units and ∼ 40 % in the paleosols. The few simulations of the MIS3 vegetation, which could be used for comparison, either address the earlier part of MIS3, with little loess sedimentation (e.g., GS12, at ∼ 44 kyr BP, for Kjellström et al., 2010, or GS15-GIS14, at ∼ 55 kyr BP, for Van Meerbeeck et al., 2011), or give results in discrepancy with the data on our area of interest (in particular for the tundra extent in central Europe; Alfano et al., 2003; Huntley et al., 2003).

In our dust calculations, by choosing the erosion wind threshold close to the lowest possible values (observed or derived as a function of soil characteristics), we aim to include all possibly important dust sources in our domain of study. However, using constant values for the threshold wind and the erosion potential implies homogeneous soil characteristics (obstacles and mineralogy), which is not very realistic. In the general case, the intensity and possibly even the location of the most active emission spots would be affected by taking into account the surface inhomogeneity, which implies variations of erosion threshold and potential across an investigated region. In our case, the main emission band determined by the climate-related conditions does correspond to surfaces favorable to deflation. Moreover, the erosion potential in this band decreases from NW towards SW, so, if taken into account, it would accentuate the emission flux gradient in Fig. 4a. Thus, Spot 2 falls in a roughly flat zone of Tertiary sediment, with high erosion potential. Spot 1 lies in a more complex area with Cretaceous sedimentary rocks westward, while eastwards outcrop less erodible Precambrian extrusive rocks, mixed with locally medium grade metamorphic ones (Asch, 2005). We note that the thickest European deposits are generally located along major river valleys (of the Seine, the Rhine, the Danube, or the Dnieper). In glacial times, these valleys used to be almost dried-out most of the year. Rich in sands and silts transported by the rivers during the snow-melting period, they constituted important deflation areas. Where the relief context favored the retention of the coarse deflated material, thick deposits have formed within a short distance downwind (e.g., Antoine

et al., 2001; Smalley et al., 2009). This explains, the exceptional thickness (for Europe) of the loess deposits at Nussloch (~ 13.5 m for the 40–15 kyr BP interval in the P4 sequence; Antoine et al., 2009), on the eastern bank of the Rhine valley, in the context of prevailing westerly winds. In general, even though periglacial braided rivers used to be important local sources for the coarse material in some of the European loess deposits, such details cannot be captured at the resolution of an AGCM. For the Stayky area, the prevailing winds are also from west–northwest (Fig. 3; see also Rousseau et al., 2007). Nevertheless, due to the relief configuration east of the Dnieper (a plain well exposed to wind erosion), no loess deposit has formed downwind in the close vicinity of the valley. The nearest loess deposits are located on the west bank of the river, and contain little of the easily deflatable coarse material from the valley, brought by rare strong easterly winds. In our reference sequence, the stratigraphic units corresponding to the 40–15 kyr BP interval only add up to ~ 6.5 m thickness. Thus, while both Nussloch and Stayky sites have recorded millennial climate variations, their sensitivity to the climate signal depended on the local relief context. At Stayky, without a strong local source upwind, the relative contribution of more remote sources as those we identify here must have been higher.

The emission flux calculations use 6-hourly winds, but even this high time series frequency does not capture the shorter episodes of strong wind, which mainly control the total amount of emitted dust. A way to compensate for that would be to lower the emission threshold. Changing this threshold from the 7 m s^{-1} value used here to 6 m s^{-1} obviously increases the mean annual flux (not shown), but only slightly widens the main emission areas, and does not affect the location of the most active spots or the relative differences between the simulated climate states.

The simulated monthly mean 10 m-winds in our investigated domain during the dusty season (Fig. 6) are in agreement with the W-NW wind direction inferred from field observations by Rozycki (1967) and Léger (1990) describing the so-called gredas, ridge-like morphology.

Considering the predominant wind direction, and the distance to our reference site, Spot 1 is particularly well placed as a source for the Stayky deposits. Dust calculations only taking into account the wind and soil humidity conditions give emission fluxes by 10 to 30 % lower in the warm GIS perturbation than in the GS reference state. Adding the vegetation effect increases the difference by another 10 to 20 %.

Spot 2 is the largest and most intense deflation area of the simulated emission band in the reference GS experiment, without as well as with the vegetation effect. In the GIS simulation, dust fluxes are only by up to 20 % smaller than in the reference state before applying the vegetation inhibition factor. The vegetation effect further reduces them by 20–30 %.

A strong difference between the GS and GIS emission fluxes all along the deflation band, particularly in the most active spots, is in agreement with the loess data. These data indicate stadial loess sedimentation rates up to 5 times higher than the interstadial ones (Rousseau et al., 2007). Thus, the key role of vegetation in modulating stadial-interstadial dust emission variations is confirmed.

Also, in both main spots, the GIS surface winds are lower than the GS ones not only on average over the dusty season (Fig. 7i), but also on average over each month of this season (not shown). This result is consistent with the grain-size variations in the Stayky loess profile, indicating a coarser sedimentation in stadial than in interstadial episodes.

Concerning the H events, our modeling experiments suggest a reduction of dust emission with respect to a stadial state. When only taking into account the wind and soil humidity effects, the simulated emission flux decrease is even stronger locally than for the interstadial. Including the effect of vegetation, less developed in a colder climate, attenuates the difference of emission fluxes between a stadial and an H event (whereas it amplifies the stadial-interstadial differences, as seen above). In our experiments, the flux ratio HE/GS is up to 10 % higher with than without the vegetation effect, but the HE fluxes remain smaller than the GS ones. This is somehow counterintuitive, because colder climates are associated with higher loess sedimentation rates, generally

interpreted as a result of stronger winds and dryer conditions, favoring both the emission and the transport of dust. This is certainly true for "cold and dry" vs. "warm and humid" climates, like glacial (loess sedimentation) vs. interglacial (no loess sedimentation) or, at a finer timescale, stadial (high loess sedimentation rate) vs. interstadial (reduced or no sedimentation). The emission attenuation suggested by our experiments for an H event compared to a stadial state can be understood if we think of the stadial – H event transition as a change from "cold and dry" to "colder and drier". Indeed, the lower dust emission fluxes in our HE experiment than in the GS one are associated with lower precipitation and weaker winds, the former favoring the dust transport, the later hindering it. Thus, a transport and deposition model would be needed to determine the net effect on the sedimentation rates in our investigated domain, and more specifically at our reference site. But even if we used such a model, loess stratigraphy offers no element to confront the results, as there is practically no way to distinguish between dust layers deposited at different rates in similarly dry conditions. In the case of interstadials, the lower emission activity is associated with wetter soil conditions, favorable to pedogenesis, and the resulting soils (well developed or in embrionary form only), are distinguishable in the sediment (Rousseau et al., 2007, 2011). In contrast, only exceptionally it is possible to find in stratigraphic profiles particular features susceptible to be associated with H events. It is the case of the millimetric sandy laminations identified in particular loess units at the Nussloch loess site, in Germany, resulted from a combination of strong wind events and coarser deposition (Lautridou et al., 1985; Derbyshire and Mellors, 1988). Otherwise, loess studies suggest that H events only can be identified as peaks in the grain-size index records (Porter and An, 1995; Antoine et al., 2001, 2009; Rousseau et al., 2002, 2007). In theory, if such records had a fine enough resolution, and the different variations could be dated with a reasonable precision, it would be possible to distinguish the sedimentation rates corresponding to the different climate episodes. In practice, to date, no loess profile allows such quantitative estimations. Qualitatively, as the sandy laminations, the grain-size peaks are interpreted as indicating episodes of particularly strong wind and coarser deposition, also reflecting

an increased relative contribution of the nearby emission areas to the deposition at the considered site.

Looking at our numerical results from this perspective, we note that for Spot 1, close to Stayky, the monthly mean emission fluxes are the highest in the month of April of the HE state (Fig. 6). Also, the average wind in April for HE in Spot 1 is directed eastward at the 850 hPa level as well as at 10 m (not shown). So, it is in the HE state, during this particular month, that Spot 1 may have the highest contribution to dust deposition at Stayky of all months and analyzed climate states. In addition, in the grid cell corresponding to Stayky, the few strongest 10 m-wind events over the year, exceeding $20\,m\,s^{-1}$ on average over 6 h, also occur in April (and in December, but this is outside the dusty season). Even though in this cell the emission dust flux in HE's month of April is lower than in the main emission spots, 20–25 $g\,m^{-2}\,month^{-1}$ only, the proximity to the deposition site makes it an important potential contributor to the Stayky sediments. Thus, our modeling results support the identification of H events in loess sequences as peaks of grain-size index.

5 Summary and conclusions

Following the Sima et al. (2009) study on the impact of North-Atlantic abrupt climate changes on dust emission in Western Europe, and the correlation proposed by Rousseau et al. (2011) between Greenland, West and East European dust records, we have focused here on the Eastern European dust sources under MIS3 climate conditions. The same simulations for a Greenland interstadial ("GIS"), a Greenland stadial ("GS") and a Heinrich event ("HE") have been used. We have combined results from these numerical experiments, and dust emission calculations at an appropriately high spatial and temporal resolution, with information from the loess site of Stayky, in Ukraine.

A band located north and northeast of the Carpathians appears as an important deflation area, potential source for the eastern European loess deposits located around

50° N latitude. Two spots are particularly active, one in Ukraine (Spot 1), the other in Poland (Spot 2). Located west–northwest from Stayky, they are well placed to be the main dust sources for our reference site.

Considering the identified deflation band as a whole, dust emission mainly occurs from February to June in the "Greenland stadial" GS experiment from March to June in the "Heinrich event" HE experiment, and from February to May in the "Greenland interstadial" GIS simulations. The beginning of the dusty season is constrained by soil humidity and snow conditions, while the end is determined by vegetation development.

In each simulated climate state, the dusty season in Spot 1 is one month earlier than for to Spot 2. This happens mainly because Spot 1 is located more south, farther away from the ice sheet, so that air temperature is higher on average. Therefore, the soil dries earlier in the year, allowing dust emission to begin, but the vegetation also develops earlier and reaches more rapidly the critical threshold above which emission is completely inhibited.

The same mechanisms are responsible for the differences of dusty season between the different simulated climate states. The main cause is again the difference of temperature, which comes, in this case, from the imposed changes in the North Atlantic sea-surface conditions.

In the main deflation band, emission fluxes are by 30 to 50 % lower in the GIS experiment than in the GS one. About half of the emission flux difference is due to the vegetation, which is better developed in the warmer climate, and thus protects more efficiently the soil from aeolian erosion. This confirms the key role of vegetation in modulating the response of dust emission intensity in Europe to the North-Atlantic millennial variability. Furthermore, the simulated weaker winds and slightly higher precipitation in interstadial conditions suggest less favorable conditions for transport than in a stadial. Our modeling results are thus qualitatively consistent with the stadial-interstadial sedimentation variations in the Stayky loess profile, and in the European loess sequences in general.

In the HE experiment, emission fluxes are generally lower than the GS ones. The simulated climate is slightly drier, but also a bit less windy over the region studied here. A transport and deposition model would be needed to evaluate the resulting change of average sedimentation rate at a loess site; the resolution and dating uncertainties of the available loess profiles do not allow a comparison with such a result anyway. It is possible however to investigate the hypothesis put forward by some loess data studies, i.e., that H events can be identified in some of the most detailed loess profiles as peaks of the grain-size index. Such peaks represent brief intervals of coarser sedimentation, due to a combination of stronger winds and increased relative contribution of the nearby vs. remote sources. Our simulations support this interpretation, pointing to the month of April of the HE experiment as the month with strongest winds in the immediate vicinity of Stayky, where some dust mobilization occurs, and highest dust emission in the main deflation Spot 1, only a few hundred kilometers away, associated with dominant 850 hPa winds directed towards our reference site.

As said above, the temporal resolution of European loess profiles is not very high; in the best cases it can get below a century for certain layers of particularly thick sediments. On the modeling side, quite a number of hypotheses on the boundary conditions must be made to simulate MIS3 climates. Also, the horizontal resolution of most AGCM experiments makes it difficult to correlate data from particular sites with numerical results. This study, using the same numerical means and methods as the one dedicated to Western Europe (Sima et al., 2009), and an approach adapted to Eastern Europe, propose another way to put together loess data and climate simulations to critically assess the modeling results, and test data interpretation. Investigating mechanisms and regional details strongly benefits from the "zoom" capacity of the LMDZ AGCM, and from analyzing the results at timescales ranging from yearly averages down to high frequency time series (6 h in our case).

Taking advantage of recent modeling advancements and results can certainly improve this work. For our future simulations we consider two main changes: forcing the AGCM with sea-surface conditions issued by MIS3 simulations with a coupled

ocean-atmosphere model, instead of the GLAMAP dataset for the LGM, and imposing a vegetation distribution consistent with the simulated glacial climates instead of the present-day distribution. Also, the effect of precipitation will be taken into account along with that of temperature in computing the vegetation changes. We also plan to simulate the entire dust cycle (emission transport and deposition), in view of a more quantitative comparison to European loess data.

Acknowledgements. This study was supported by the French Agence Nationale pour la Recherche (ANR) through the ACTES project ANR-08-BLAN-0227/CSD-6. The simulations were performed using HPC resources of the Commissariat à l'Energie Atomique, France.

The publication of this article is financed by CNRS-INSU.

References

Alfano, M. J., Barron, E. J., Pollard, D., Huntley, B., and Allen, J. R. M.: Comparison of climate model results with European vegetation and permafrost during oxygen isotope stage three, Quaternary Res., 59, 97–107, doi:10.1016/s0033-5894(02)00012-1, 2003.

Alvarez-Solas, J. and Ramstein, G.: On the triggering mechanism of Heinrich events, P. Natl. Acad. Sci. USA, 108, E1359–E1360, doi:10.1073/pnas.1116575108, 2011.

Antoine, P., Rousseau, D. D., Zöller, L., Lang, A., Munaut, A. V., Hatté, C., and Fontugne, M.: High-resolution record of the last interglacial-glacial cycle in the loess palaeosol sequences of Nussloch (Rhine Valley-Germany), Quaternary Int., 76–77, 211–229, 2001.

Antoine, P., Catt, J., Lautridou, J. P., and Somme, J.: The loess and coversands of northern France and southern England, J. Quaternary Sci., 18, 309–318, 2003a.

Antoine, P., Coutard, J. P., Gibbard, P., Hallegouët, B., Lautridou, J. P., and Ozouf, J. C.: The Pleistocene rivers of the English Channel region, J. Quaternary Sci., 18, 227–243, 2003b.

Antoine, P., Rousseau, D. D., Moine, O., Kunesch, S., Hatté, C., Lang, A., Tissoux, H., and Zöller, L.: Rapid and cyclic aeolian deposition during the Last Glacial in European loess: a high-resolution record from Nussloch, Germany, Quaternary Sci. Rev., 28, 2955–2973, doi:10.1016/j.quascirev.2009.08.001, 2009.

Arzel, O., England, M. H., de Verdiere, A. C., and Huck, T.: Abrupt millennial variability and interdecadal-interstadial oscillations in a global coupled model: sensitivity to the background climate state, Clim. Dynam., 39, 259–275, doi:10.1007/s00382-011-1117-y, 2012.

Asch, K.: The 1 : 5 Million Geological Map of Europe and Adjacent Areas, BRG (Bundesanstalt für Geowissenschaften und Rohstoffe), Hannover, Germany, 2005.

Auffret, J. P.: Les formations sédimentaires holocènes du domaine prélittoral picard, Bulletin de l'Association française pour l'Etude du Quaternaire, 1–2, 34, 1980.

Auffret, J. P., Horn, R., Larsonneur, C., Curry, D., and Smith, A. J.: La Manche orientale, carte des paléovallées et des bancs sableux, Bureau des recherches Géologiques et Minières, Orléans, 1982.

Balkanski, Y., Schulz, M., Claquin, T., Moulin, C., and Ginoux, P.: The formulation of dust emissions on global scale: Formulation and validation using satellite retrievals, in: Emissions of Atmospheric Trace Compounds, edited by: Granier, C., Artaxo, P., and Reeves, C., Kluwer Academic Publishers, Dordrecht, The Netherlands, 239–267, 2004.

Bard, E., Menot-Combes, G., and Rostek, F.: Present status of radiocarbon calibration and comparison records based on Polynesian corals and Iberian Margin sediments, Radiocarbon, 46, 1189–1202, 2004.

Barron, E. and Pollard, D.: High-resolution climate simulations of oxygen istopose stage 3 in Europe, Quaternary Res., 58, 296–309, 2002.

Berger, A. L.: Long-term variations of caloric insolation resulting from the Earth's orbital elements, Quaternary Res., 9, 139–167, 1978.

Berger, A. and Loutre, M. F.: Insolation values for the climate of the last 10 millions years, J. Quaternary Sci., 10, 297–317, 1991.

Braconnot, P.: Modeling the last glacial maximum and mid-holocene, C. R. Geosci., 336, 711–719, doi:10.1016/j.crte.2003.12.023, 2004.

Brandefelt, J., Kjellström, E., Näslund, J.-O., Strandberg, G., Voelker, A. H. L., and Wohlfarth, B.: A coupled climate model simulation of Marine Isotope Stage 3 stadial climate, Clim. Past, 7, 649–670, doi:10.5194/cp-7-649-2011, 2011.

Broecker, W., Bond, G., Klas, M., Clark, E., and McManus, J.: Origin of the northern Atlantic's Heinrich events, Clim. Dynam., 6, 265–273, 1992.

Capron, E., Landais, A., Chappellaz, J., Schilt, A., Buiron, D., Dahl-Jensen, D., Johnsen, S. J., Jouzel, J., Lemieux-Dudon, B., Loulergue, L., Leuenberger, M., Masson-Delmotte, V., Meyer, H., Oerter, H., and Stenni, B.: Millennial and sub-millennial scale climatic variations recorded in polar ice cores over the last glacial period, Clim. Past, 6, 345–365, doi:10.5194/cp-6-345-2010, 2010.

Cortijo, E., Labeyrie, L., Vidal, L., Vautravers, M., Chapman, M., Duplessy, J. C., Elliot, M., Arnold, M., Turon, J. L., and Auffret, G.: Changes in sea surface hydrology associated with Heinrich event 4 in the North Atlantic Ocean between 40° and 60° N, Earth Planet. Sc. Lett., 146, 29–45, doi:10.1016/s0012-821x(96)00217-8, 1997.

Dansgaard, W., Johnsen, S. J., Clausen, H. B., Dahi-Jensen, D., Gundestrup, N. S., Hammer, C. U., Hvidberg, C. S., Steffensen, J. P., Sveinbjöprnsdottir, A. E., Jouzel, J., and Bond, G.: Evidence for general instability of past climate from a 250-kyr ice-core record, Nature, 364, 218–220, 1993.

de Beaulieu, J. L. and Reille, M.: The pollen sequence of Les Échets (France) : a new element for the chronology of the Upper Pleistocene., Geogr. Phys. Quatern., 38, 3–9, 1984.

de Beaulieu, J. L. and Reille, M.: The last climatic cycle at La Grande Pile (Vosges, France) a new pollen profile, Quaternary Sci. Rev., 11, 431–438, 1992.

Derbyshire, E. and Mellors, T. W.: Geological and geotechnical characteristics of some loess and loessic soils from China and Britain – a comparison, Eng. Geol., 25, 135–175, doi:10.1016/0013-7952(88)90024-5, 1988.

Ducoudré, N. I., Laval, K., and Perrier, A.: Sechiba, a New Set of Parameterizations of the Hydrologic Exchanges at the Land Atmosphere Interface within the LMD Atmospheric General-Circulation Model, J. Climate, 6, 248–273, 1993.

Ehlers, J., Gibbard, P., and Hughes, P. D.: Quaternary Glaciations – Extent and Chronology, Development in Quaternary Studies, edited by: van der Meer, J., Elsevier, Amsterdam, 1126 pp., 2011.

Fryrear, D. W.: Soil Cover and Wind Erosion, T. ASAE, 28, 781–784, 1985.

Fuchs, M., Kreutzer, S., Rousseau, D. D., Antoine, P., Hatté, C., Lagroix, F., Moine, O., Gauthier, C., Svoboda, J., and Lenka, L.: The loess sequence of Dolni Vestonice, Czech Republic: a new OSL-based chronology of the last climatic cycle, Boreas, online first: doi:10.1111/j.1502-3885.2012.00299.x, 2012.

Gerasimenko, N. and Rousseau, D. D.: Stratigraphy and paleoenvironments of the last Pleniglacial in the Kyiv loess region (Ukraine), Quaternaire, 19, 293–307, 2008.

Haase, D., Fink, J., Haase, G., Ruske, R., Pecsi, M., Richter, H., Altermann, M., and Jager, K. D.: Loess in Europe - its spatial distribution based on a European Loess Map, scale 1 : 2,500,000, Quaternary Sci. Rev., 26, 1301–1312, 2007.

Haesaerts, P., Borziak, I., Chirica, V., Damblon, F., Koulakovska, L., and van der Plicht, J.: The east Carpathian loess record: a reference for the middle and late pleniglacial stratigraphy in central Europe, Quaternaire, 14, 163–188, 2003.

Hatté, C. and Guiot, J.: Palaeoprecipitation reconstruction by inverse modelling using the isotopic signal of loess organic matter: application to the Nussloch loess sequence (Rhine Valley, Germany), Clim. Dynam., 25, 315–327, doi:10.1007/s00382-005-0034-3, 2005.

Hatté, C., Fontugne, M., Rousseau, D. D., Antoine, P., Zöller, L., Tisnérat-Laborde, N., and Bentaleb, I.: δ^{13}C variations of loess organic matter as a record of the vegetation response to climatic changes during the Weichselian, Geology, 26, 583–586, 1998.

Heinrich, H.: Origin and consequences of cyclic ice rafting in the Northeast Atlantic Ocean during the past 130 000 years, Quaternary Res., 29, 142–152, 1988.

Hostetler, S. W., Clark, P. U., Bartlein, P. J., Mix, A. C., and Pisias, N. J.: Atmospheric transmission of North Atlantic Heinrich events, J. Geophys. Res., 104, 3947–3952, 1999.

Huntley, B., Alfano, M. J., Allen, J. R. M., Pollard, D., Tzedakis, P. C., de Beaulieu, J. L., Grüger, E., and Watts, B.: European vegetation during marine oxygen isotope stage-3, Quaternary Res., 59, 195–212, 2003.

Jost, A., Lunt, D., Kageyama, M., Abe-Ouchi, A., Peyron, O., Valdes, P. J., and Ramstein, G.: High-resolution simulations of the last glacial maximum climate over Europe: a solution to discrepancies with continental palaeoclimatic reconstructions?, Clim. Dynam., 24, 577–590, doi:10.1007/s00382-005-0009-4, 2005.

Juvigné, E.: Contribution à la connaissance de la stratigraphie au Quaternaire par l'étude des minéraux denses transparents entre l'Eifel et le Massif Central français et plus particulièrement en Belgique, Département de Géographie, Liège, 235 pp., 1976.

Kjellstrom, E., Brandefelt, J., Naslund, J. O., Smith, B., Strandberg, G., Voelker, A. H. L., and Wohlfarth, B.: Simulated climate conditions in Europe during the marine isotope stage 3 stadial (Vol. 39, p. 436, 2010), Boreas, 40, p. 210, doi:10.1111/j.1502-3885.2010.00155.x, 2011.

Krinner, G., Viovy, N., de Noblet-Ducoudre, N., Ogee, J., Polcher, J., Friedlingstein, P., Ciais, P., Sitch, S., and Prentice, I. C.: A dynamic global vegetation model for studies of the coupled atmosphere-biosphere system, Global Biogeochem. Cy., 19, Gb1015, doi:10.1029/2003gb002199, 2005.

Kukla, G.: Pleistocene land-sea correlations. 1. Europe, Earth-Sci. Rev., 13, 307–374, 1977.

Laurent, B., Marticorena, B., Bergametti, G., Chazette, P., Maignan, F., and Schmechtig, C.: Simulation of the mineral dust emission frequencies from desert areas of China and Mongolia using an aerodynamic roughness length map derived from the POLDER/ADEOS 1 surface products, J. Geophys. Res.-Atmos., 110, D18S0, doi:10.1029/2004jd005013, 2005.

Lautridou, J. P., Sommé, J., Heim, J., Puisségur, J. J., and Rousseau, D. D.: La stratigraphie des loess et formations fluviatiles d'Achenheim (Alsace) : Nouvelles données bioclimatiques et corrélations avec les séquences Pléistocènes de la France du Nord-Ouest. in: Dynamical and Chronological Relations Between Glacial and Periglacial Deposits, edited by: Campy, M., Bulletin de l'Association française pour l'étude du Quaternaire, 22–23, 125–132, 1985.

Léger, M.: Loess Landforms, Quaternary Int., 7/8, 53–61, 1990.

Marticorena, B. and Bergametti, G.: Two-year simulations of seasonal and interannual changes of the Saharan dust emissions, Geophys. Res. Lett., 23, 1921–1924, 1996.

Martinson, D. G., Pisias, N. G., Hays, J. D., Imbrie, J., Moore, T. C., and Shackleton, N. J.: Age dating and the orbital theory of the Ice ages: development of a high-resolution 0 to 300 000-year chronostratigraphy, Quaternary Res., 27, 1–29, 1987.

Merkel, U., Prange, M., and Schulz, M.: ENSO variability and teleconnections during glacial climates, Quaternary Sci. Rev., 29, 86–100, doi:10.1016/j.quascirev.2009.11.006, 2010.

Moine, O., Rousseau, D. D., and Antoine, P.: The impact of Dansgaard-Oeschger cycles on the loessic environment and malacofauna of Nussloch (Germany) during the Upper Weichselian, Quaternary Res., 70, 91–104, doi:10.1016/j.yqres.2008.02.010, 2008.

Müller, U. C., Pross, J., and Bibus, E.: Vegetation response to rapid climate change in Central Europe during the past 140 000 yr based on evidence from the Füramoos pollen record, Quaternary Res., 59, 235–245, 2003.

North Greenland Ice Core Project Members: High-resolution record of Northern Hemisphere climate extending into the last interglacial period, Nature, 431, 147–151, 2004.

Peltier, W. R.: Ice-age paleotopography, Science, 265, 195–201, 1994.

Petit, J. R., Jouzel, J., Raynaud, D., Barkov, N. I., Barnola, J. M., Basile, I., Bender, M., Chappellaz, J., Davis, M., Delaygue, G., Delmotte, M., Kotlyakov, V. M., Legrand, M., Lipenkov, V. Y., Lorius, C., Pépin, L., Ritz, C., Saltzman, E., and Stievenard, M.: Climate and atmospheric history of the past 420 000 years from the Vostok ice core, Antarctica, Nature, 399, 429–436, 1999.

Peyron, O., Guiot, J., Cheddadi, R., Tarasov, P., Reille, M., De Beaulieu, J. L., Bottema, S., and Andrieu, V.: Climatic reconstruction in Europe for 18 000 yr BP from pollen data, Quaternary Res., 49, 183–196, 1998.

Porter, S. C. and An, Z. S.: Correlation between climate events in the North Atlantic and China during the last glaciation, Nature, 375, 305–308, 1995.

Renssen, H. and Bogaart, P. W.: Atmospheric variability over the ∼14.7 kyr BP stadial-interstadial transition in the North Atlantic region as simulated by an AGCM, Clim. Dynam., 20, 301–313, 2003.

Rousseau, D. D., Puisségur, J. J., and Lautridou, J. P.: Biogeography of the Pleistocene Pleniglacial malacofaunas in Europe. Stratigraphic and climatic implications, Palaeogeogr. Palaeocl., 80, 7–23, 1990.

Rousseau, D. D., Gerasimenko, N., Matviischina, Z., and Kukla, G.: Late Pleistocene environments of the Central Ukraine, Quaternary Res., 56, 349–356, 2001.

Rousseau, D. D., Antoine, P., Hatté, C., Lang, A., Zöller, L., Fontugne, M., Ben Othman, D., Luck, J. M., Moine, O., Labonne, M., Bentaleb, I., and Jolly, D.: Abrupt millennial climatic changes from Nussloch (Germany) Upper Weichselian eolian records during the Last Glaciation, Quaternary Sci. Rev., 21, 1577–1582, 2002.

Rousseau, D. D., Kukla, G., and McManus, J.: What is what in the ice and the ocean?, Quaternary Sci. Rev., 25, 2025–2030, 2006.

Rousseau, D. D., Sima, A., Antoine, P., Hatté, C., Lang, A., and Zöller, L.: Link between European and North Atlantic abrupt climate changes over the last glaciation, Geophys. Res. Lett., 34, L22713, doi:10.1029/2007gl031716, 2007.

Rousseau, D.-D., Antoine, P., Gerasimenko, N., Sima, A., Fuchs, M., Hatté, C., Moine, O., and Zoeller, L.: North Atlantic abrupt climatic events of the last glacial period recorded in Ukrainian loess deposits, Clim. Past, 7, 221–234, doi:10.5194/cp-7-221-2011, 2011.

Rozycki, S. Z.: Le sens des vents portant la poussière de loess à la lumière de l'analyse des formes d'accumulation du loess en Bulgarie et en Europe Centrale, Revue de Géomorphologie dynamique, 1, 1–9, 1967.

Sarnthein, M., Gersonde, R., Niebler, S., Pflaumann, U., Spielhagen, R., Thiede, J., Wefer, G., and Weinelt, M.: Overview of Glacial Atlantic Ocean Mapping (GLAMAP 2000), Paleoceanography, 18, 1030, doi:10.1029/2002PA000769, 2003.

Siddall, M., Rohling, E. J., Thompson, W. G., and Waelbroeck, C.: Marine isotope stage 3 sea level fluctuations: Data synthesis and new outlook, Rev. Geophys., 46, RG4003 doi:10.1029/2007rg000226, 2008.

Sima, A., Rousseau, D. D., Kageyama, M., Ramstein, G., Schulz, M., Balkanski, Y., Antoine, P., Dulac, F., and Hatté, C.: Imprint of North-Atlantic abrupt climate changes on western European loess deposits as viewed in a dust emission model, Quaternary Sci. Rev., 28, 2851–2866, doi:10.1016/j.quascirev.2009.07.016, 2009.

Smalley, I., O'Hara-Dhand, K., Wint, J., Machalett, B., Jary, Z., and Jefferson, I.: Rivers and loess: the significance of long river transportation in the complex event-sequence approach to loess deposit formation, Quaternary Int., 198, 7–18, doi:10.1016/j.quaint.2008.06.009, 2009.

Van Meerbeeck, C. J., Renssen, H., Roche, D. M., Wohlfarth, B., Bohncke, S. J. P., Bos, J. A. A., Engels, S., Helmens, K. F., Sanchez-Goni, M. F., Svensson, A., and Vandenberghe, J.: The nature of MIS 3 stadial-interstadial transitions in Europe: new insights from model-data comparisons, Quaternary Sci. Rev., 30, 3618–3637, doi:10.1016/j.quascirev.2011.08.002, 2011.

Wang, X., Ma, Y., Chen, H., Wen, G., Chen, S., Tao, Z., and Chung, Y. S.: The relation between sandstorms and strong winds in Xinjiang, China, Water Air Soil Poll., 3, 67–79, 2003.

Woillard, G.: Grande pile peat bog: a continuous pollen record for the last 140 000 years, Quaternary Res., 9, 1–21, 1978.

Woillez, M.-N., Kageyama, M., Krinner, G., de Noblet-Ducoudré, N., Viovy, N., and Mancip, M.: Impact of CO_2 and climate on the Last Glacial Maximum vegetation: results from the ORCHIDEE/IPSL models, Clim. Past, 7, 557–577, doi:10.5194/cp-7-557-2011, 2011.

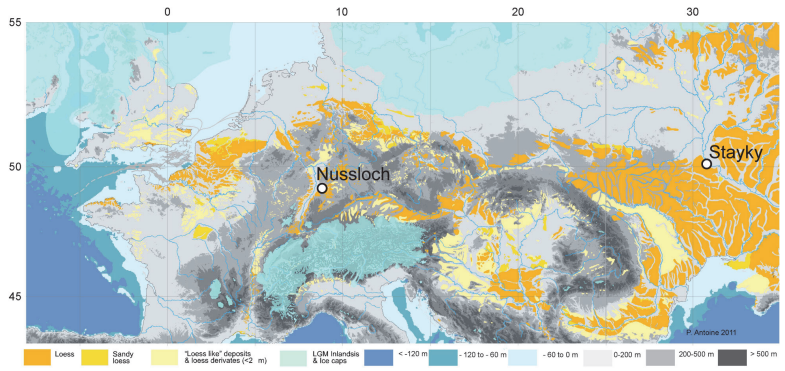

Fig. 1. Map of the thickest European loess deposits (in yellow), in the context of the Last Glacial Maximum (21 kyr BP) ice sheets (light blue) and sea level (unpublished map by P. Antoine, 2011, after data from compilations kindly provided by D. Haase from Haase et al., 2007, and J. Ehlers from Ehlers et al., 2011).

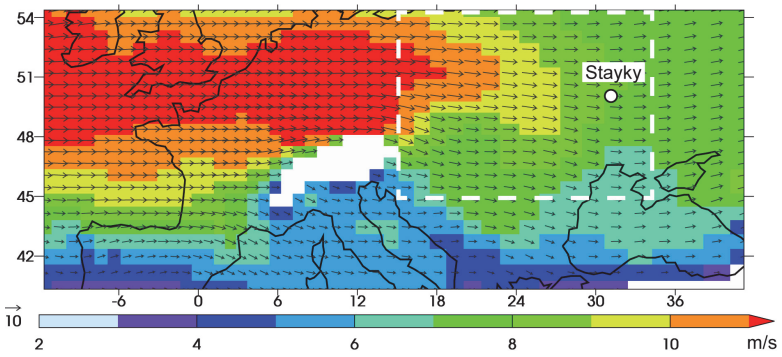

Fig. 2. Mean annual 850 hPa wind speed and direction for the reference GS state (modified from Rousseau et al., 2011). The area investigated in this study stretches between 15°–35° E and 45°–55° N.

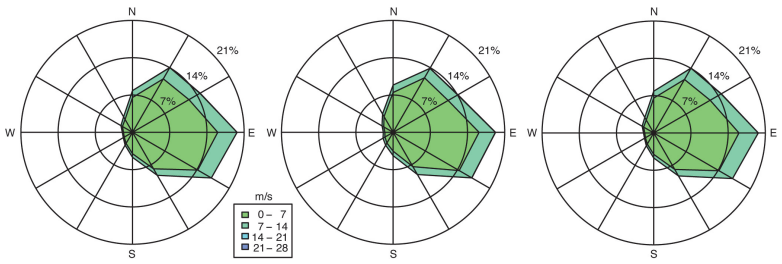

Fig. 3. 10 m-wind roses derived from 6-hourly 10 m winds at Stayky for 20 yr of simulation for each of the three climate states. Relevant winds for dust emission are those exceeding the threshold erosion wind speed, 7 m s^{-1} in this study. Winds below 14 m s^{-1} are much more frequent than those above 14 m s^{-1} (which cannot even be seen on the plots); cf. Sima et al. (2009), they determine most of the emitted amount of dust.

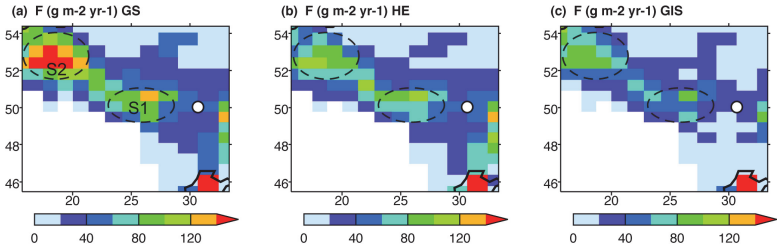

Fig. 4. Annual means of dust emission fluxes F ($g m^{-2} yr^{-1}$) for the three simulated climate states: GS (left), HE (middle), and GIS (right). The flux calculation includes the vegetation effect. Emission mainly occurs in a NW–SE band, with two most active spots, S1 and S2.

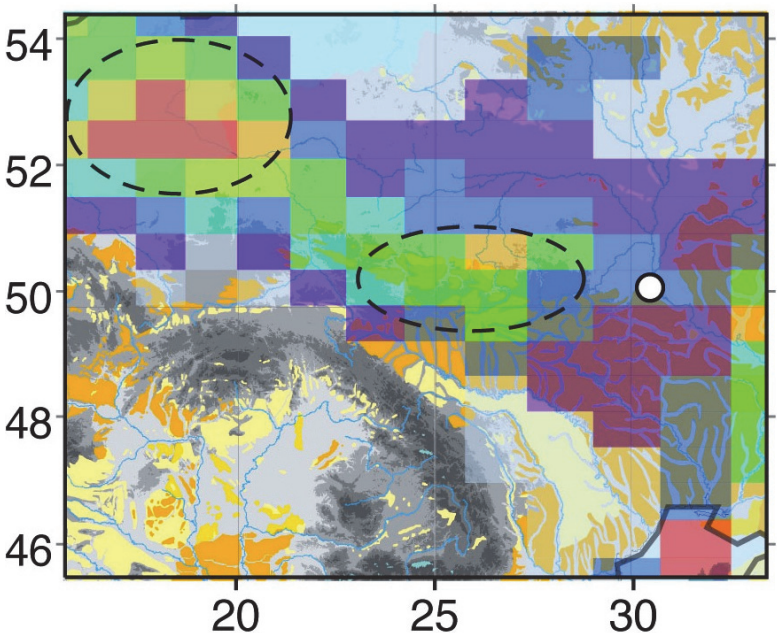

Fig. 5. Annual mean of dust emission fluxes for GS (Fig. 4a) superimposed on the topographic map.

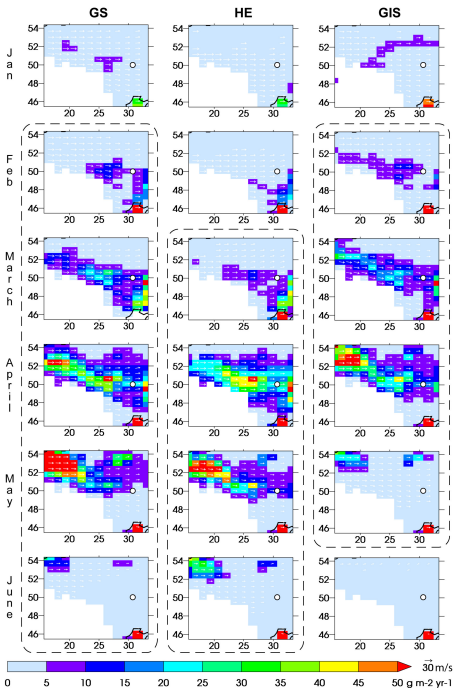

Fig. 6. Monthly means of dust emission fluxes outside the Carpathians in the three simulated climate states for January to June. Wherever the slightest emission occurs, the monthly average wind vectors at 850 hPa indicate the direction in which the dust is must likely transported. Little or no dust is emitted in this area in the rest of the year.

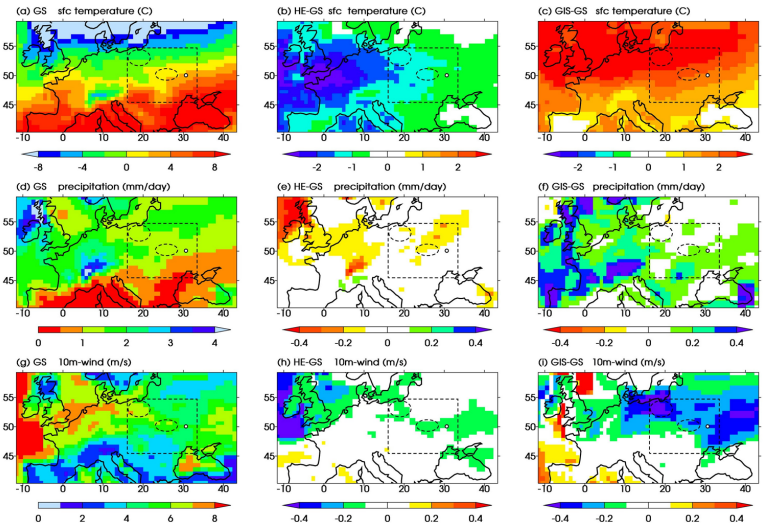

Fig. 7. February to June averages of 2 m-temperature **(a–c)**, precipitation **(d–f)** and 10 m-wind **(g–i)** for the GS state (left column), and anomalies HE-GS (center column) and GIS-GS (right column).

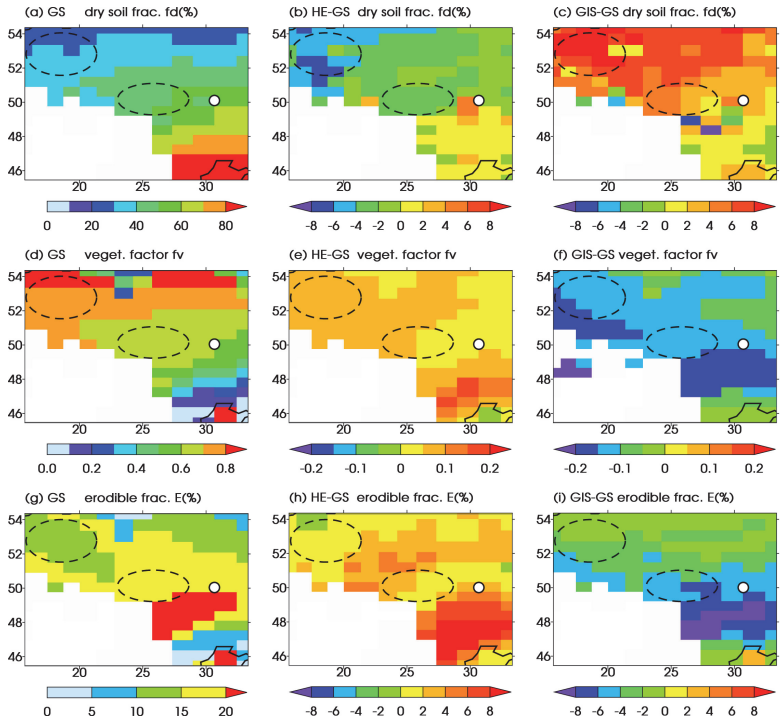

Fig. 8. Averages over the dust emission period (February to June) for dry soil fraction f_d, vegetation factor f_v and erodible soil fraction E in the GS state (left column), and anomalies HE-GS (center) and GIS-GS (right).

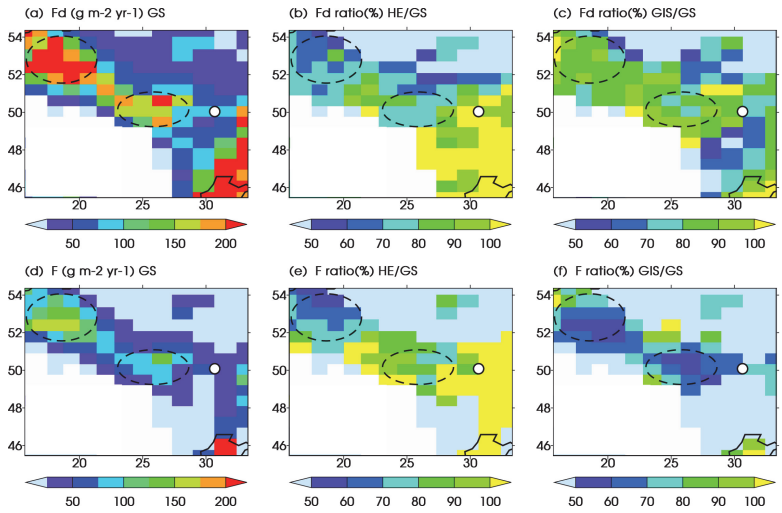

Fig. 9. Mean annual dust fluxes in the reference climate state GS (left) and ratios of dust fluxes HE/GS (center) and GIS/GS (right), without **(a–c)** and with **(d–f)** vegetation effect.

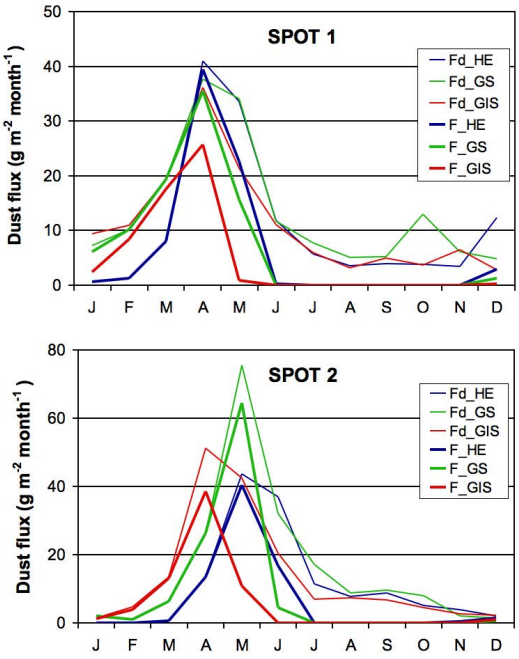

Fig. 10. Annual cycle of emitted dust flux averaged on each of the main deflation spots in the three simulated climate states, without (F_d) and with vegetation effect (F).